

# Role of Defects in Swelling and Creep of Irradiated SiC

---

## Reactor Concepts

Izabela Szlufarska

University of Wisconsin, Madison

**In collaboration with:**

Oak Ridge National Laboratory

Yutai Katoh, Federal POC  
Rich Reister, Technical POC

## Final Report

**Project Title:** Role of defects in swelling and creep of irradiated SiC

**Covering Period:** 09/01/2012 – 08/31/2015

**Date of Report:** 1/16/2016

**Recipient:** University of Wisconsin  
Madison, WI 53706

**Contract Number:** 00089350

**Project Number:** 12-3357

**Subcontractors:** N/A

**Other Partners:** N/A

**Contact(s):** Principal Investigator: Izabela Szlufarska  
[szlufarska@wisc.edu](mailto:szlufarska@wisc.edu)

Co-Principal Investigators: Paul Voyles ([voyles@engr.wisc.edu](mailto:voyles@engr.wisc.edu))  
Kumar Sridharan ([kumar.sridharan@wisc.edu](mailto:kumar.sridharan@wisc.edu))  
Yutai Katoh ([katohy@ornl.gov](mailto:katohy@ornl.gov))

**Project Team:** Technical Point of Contact – Yutai Katoh

## Table of Content

<b>1</b>	<b>Introduction.....</b>	<b>3</b>
<b>2</b>	<b>Ion irradiation experiments .....</b>	<b>3</b>
2.1	<i>Experimental approach.....</i>	3
2.1.1	<i>Ion-irradiation .....</i>	3
2.1.2	<i>XRD measurements.....</i>	6
2.2	<i>Swelling results by XRD .....</i>	6
2.2.1	<i>Total normal strain vs. true normal strain.....</i>	8
2.2.2	<i>XRD data modeling.....</i>	9
2.3	<i>Discussion of swelling in SiC as measured by XRD.....</i>	10
2.4	<i>Summary of results .....</i>	11
<b>3</b>	<b>Imaging of defects in ion irradiated SiC.....</b>	<b>11</b>
3.1	<i>Conventional TEM characterization of Ion- and neutron-irradiated SiC .....</i>	12
3.2	<i>LAADF STEM characterization of ion-irradiated SiC .....</i>	17
<b>4</b>	<b>Defect modeling.....</b>	<b>18</b>
4.1	<i>Cluster dynamics (CD) method.....</i>	19
4.2	<i>CD model with known physical parameters for SiC.....</i>	19
4.2.1	<i>Formulation and assumptions of the model.....</i>	19
4.2.2	<i>Parameters of the model .....</i>	21
4.2.3	<i>Results .....</i>	22
4.3	<i>Effects of new physical phenomena in irradiated SiC on predictions of the CD model</i> <i>23</i>	
4.3.1	<i>Physical phenomena that may be present in irradiated SiC.....</i>	23
4.3.2	<i>Results of the adjusted model.....</i>	24
<b>5</b>	<b>Characterization of neutron irradiated SiC .....</b>	<b>26</b>
5.1	<i>Evaluation of neutron irradiation creep .....</i>	26
5.2	<i>Microstructural evolution under irradiation with applied stress .....</i>	27
5.3	<i>Possible creep mechanism .....</i>	29
5.4	<i>Summary of results .....</i>	29
<b>6</b>	<b>Publications resulting from this work.....</b>	<b>29</b>
<b>7</b>	<b>References.....</b>	<b>30</b>

## 1 Introduction

Silicon carbide is a promising cladding material because of its high strength and relatively good corrosion resistance. However, SiC is brittle and therefore SiC-based components need to be carefully designed to avoid cracking and failure by fracture. In design of SiC-based composites for nuclear reactor applications it is essential to take into account how mechanical properties are affected by radiation and temperature, or in other words, what strains and stresses develop in this material due to environmental conditions. While thermal strains in SiC can be predicted using classical theories, radiation-induced strains are much less understood. In particular, it is critical to correctly account for radiation swelling and radiation creep, which contribute significantly to dimensional instability of SiC under radiation. Swelling typically increases logarithmically with radiation dose and saturates at relatively low doses (damage levels of a few dpa). Consequently, swelling-induced stresses are likely to develop within a few months of operation of a reactor. Radiation-induced volume swelling in SiC can be as high as 2%, which is significantly higher than the cracking strain of 0.1% in SiC. Swelling-induced strains will lead to enormous stresses and fracture, unless these stresses can be relaxed via some other mechanism. An effective way to achieve stress relaxation is via radiation creep.

Although it has been hypothesized that both radiation swelling and radiation creep are driven by formation of defect clusters, existing models for swelling and creep in SiC are limited by the lack of understanding of specific defects that form due to radiation in the range of temperatures relevant to fuel cladding in light water reactors (LWRs) (<1000°C) [1, 2]. For example, defects that can be detected with traditional transmission electron microscopy (TEM) techniques account only for 10-45% of the swelling measured in irradiated SiC. Here, we have undertaken an integrated experimental and modeling effort to discover the previously invisible defects in irradiated SiC and to determine the contributions of these defects to radiation swelling. Knowledge of the most stable defect structures and the rate controlling processes during defect evolution is essential for development of predictive models for swelling and creep as a function of temperature and radiation dose. This research has been enabled by state-of-the-art imaging techniques, such as the aberration corrected scanning transmission electron microscopy (STEM) (FEI TITAN) closely coupled with multi-scale models of stable defect clusters and their evolution.

## 2 Ion irradiation experiments

### 2.1 *Experimental approach*

#### 2.1.1 *Ion-irradiation*

{0001} single crystal, hexagonal 4H-SiC ( $a = 3.073 \text{ \AA}$ ,  $c = 10.053 \text{ \AA}$ ), n-doped,  $4.1^\circ$  off towards  $[11\bar{2}0] \pm 0.5^\circ$ , with low micropipe and double-side polish from Cree and was selected for investigating swelling by X-Ray diffraction (XRD). Single-crystal was selected for ease in strain and swelling measurements by XRD and for minimizing defect density in the virgin material for TEM investigations.

To simulate neutron irradiation, 4H-SiC was irradiated at 600 °C, 800 °C, and 950 °C by 3.15 MeV  $C^{2+}$  up to 0.4 dpa and 1 MeV  $Kr^+$  at 600 °C and 800 °C up to 0.4 dpa and 0.8 dpa. Irradiations were

performed at conditions at which BSDs are expected to form without introducing much strain [3] (see Fig. 2.1).

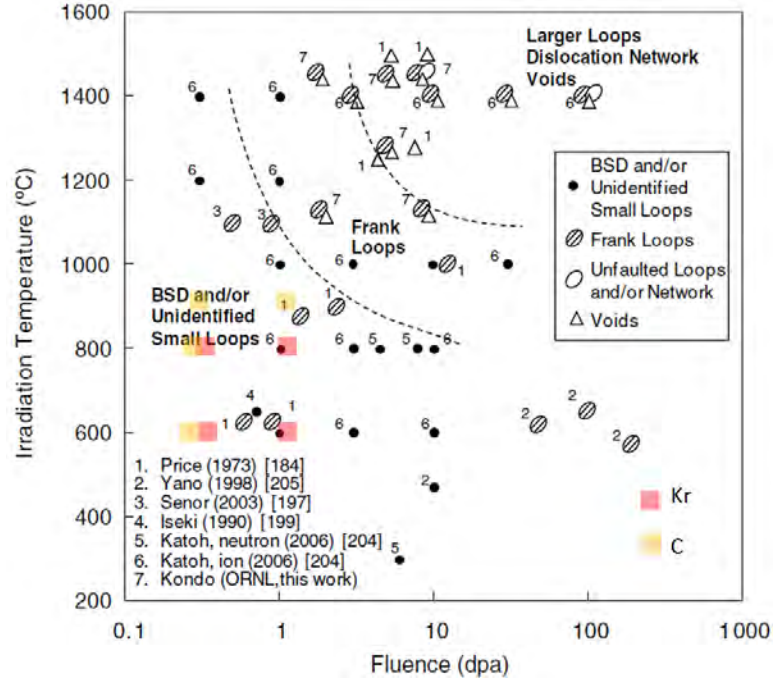


**Figure 2.1** Summary of the micro- and nano-structural development in cubic SiC after neutron and self-ion irradiation (adapted from Ref. [3]). Red and yellow squares indicate the conditions of 1 MeV Kr<sup>+</sup> and 3.15 MeV C<sup>2+</sup> irradiation of 3C-SiC and 4H-SiC, respectively, in the present study.

Carbon irradiation was performed using the 1.7 MV tandem accelerator at the University of Wisconsin, Madison under the following conditions: 3.15 MeV C<sup>2+</sup> (projected range  $R_p = 2.23 \mu\text{m} \pm 0.11 \mu\text{m}$ ) up to a fluence of  $5.14 \times 10^{16} \text{ C/cm}^2$  which corresponds to 0.4 dpa at the depth of 1  $\mu\text{m}$  (see Fig. 2.2, assuming threshold displacement energies of 20 eV and 35 eV for C and Si [4], respectively). For damage level calculations, the method proposed by Stoller *et al.* [5] was employed. Based on this, the maximum carbon concentration was about 3 at.% with a majority of the C interstitials located at the end of the irradiation range. The average current was about 4  $\mu\text{A}$ , and the flux was kept at a level of  $6.5 \times 10^{12} \text{ C/(cm}^2\text{s)}$ , resulting in a damage rate of  $5 \times 10^{-5} \text{ dpa/s}$ . The beam was rastered (64 Hz horizontally, 517 Hz vertically) over the entire irradiation area, and its uniformity was controlled by an infrared camera. Sample temperature, controlled by two thermocouples attached diagonally to the sample holder, was attained by external and beam heating with fluctuations of  $\pm 20^\circ\text{C}$ . The background pressure during irradiation was kept around  $10^{-6} \text{ Torr}$ .

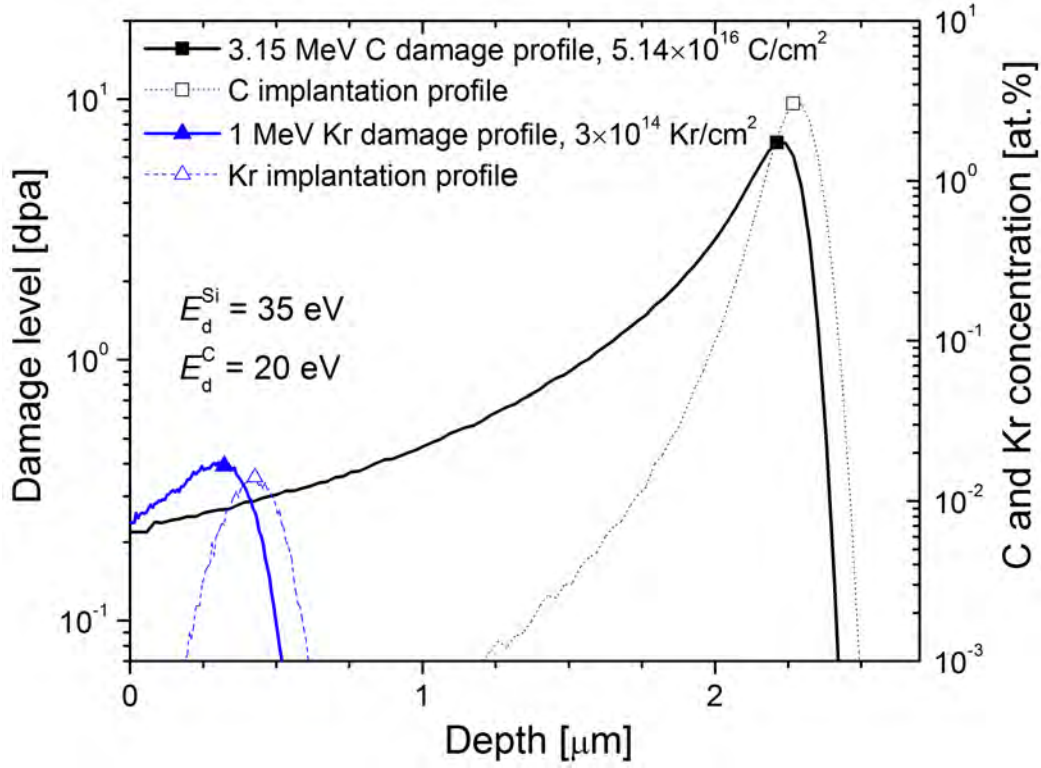


**Figure 2.2** Damage and C and Kr ion distributions in SiC irradiated with 3.15 MeV C and 1 MeV Kr ions to a damage level of 0.4 dpa at the depth of 1  $\mu\text{m}$  and peak, respectively. Calculations were performed using SRIM-2013[6], assuming the displacement threshold energies to be 20 eV for C and 35 eV for Si.

1 MeV Kr-irradiations ( $R_p = 0.4 \mu\text{m} \pm 0.09 \mu\text{m}$ ) were performed at the University of Illinois, Urbana-Champaign, Frederick Seitz Material Research Laboratory using an HVEE van der Graaf accelerator. The irradiations were conducted up to a fluence of either  $3 \times 10^{14} \text{ Kr/cm}^2$  or  $6 \times 10^{14} \text{ Kr/cm}^2$ , which corresponds to 0.4 dpa and 0.8 dpa at the damage peak, respectively (see Fig. 2.2). The maximum Kr concentration was about 0.03 at.% (for  $6 \times 10^{14} \text{ Kr/cm}^2$ ), which does not alter the stoichiometry of the implanted SiC samples. The implantation spot was  $6 \times 6 \text{ mm}^2$ , and the flux varied between  $1.4 \times 10^{12} \text{ Kr/(cm}^2\text{s)}$  and  $3 \times 10^{12} \text{ Kr/(cm}^2\text{s)}$  (current 170 nA) yielding a damage rate of  $1.7 \times 10^{-3} \text{ dpa/s}$  to  $4 \times 10^{-3} \text{ dpa/s}$ . The background pressure was about  $5 \times 10^{-7} \text{ Torr}$ , and the sample temperature was measured by a K-type thermocouple attached to the sample holder. The temperature uncertainty was within  $\pm 5^\circ\text{C}$ . The same method of damage level calculation was employed as for  $\text{C}^{2+}$  irradiation. During the irradiation, all samples were secured to the sample stage using silver paint, but only one sample was irradiated at a time while the other three were kept heated during this period. Once the desired fluence was reached, the beam was shifted to the next sample. In all cases, the beam was perpendicular to the sample surface, and ion channeling was avoided as a consequence of the  $4.1^\circ$  off-cut angle of the virgin material.

### 2.1.2 XRD measurements

Ion-induced strain and point defect swelling were measured by means of XRD. The measurements of single crystal 4H-SiC were conducted at room temperature with a PANalytical X'pert PRO diffractometer in Bragg (reflection) geometry utilizing Cu-K<sub>α1</sub> radiation ( $\lambda = 0.154056$  nm) in combination with a hybrid monochromator consisting of a closely coupled X-ray mirror and a 4-bounce Ge 220 monochromator (18 arcsec resolution). By adjusting azimuthal and polar angles, the sample was precisely oriented in order to align a given crystallographic direction exactly with the diffraction vector. The strain spectra were measured with the [11 $\bar{2}$ 0] direction (off-cut angle direction) in the detection plane, i.e., parallel to the projection of the incident beam on the sample surface. The alignment was performed on the crystal planes instead of the surface, which reduced the axial divergence. The azimuthal orientation was with the off-cut angle direction parallel to the incident beam direction to avoid the above-mentioned axial divergence problem. The  $2\theta$ - $\omega$  scans were taken at the (0004) pole with  $0.001^\circ$  steps, 0.5 s per step. In the case of the off-cut samples used in this research, the XRD spectra were measured at an angle  $\alpha = 4.1^\circ$  from the reciprocal lattice vector corresponding to the (0004) pole. The value of the total normal strain was calculated from the equation

$$\varepsilon_N^{tot} = \frac{\Delta c}{c} = -\Delta\theta \cot\theta_B \quad \text{Equation 2.1}$$

where  $\Delta\theta$  is the difference between the diffraction angle  $\theta = (2\theta)/2$  and the Bragg angle  $\theta_B$ , and  $c = 10.053$  Å.

To determine the fraction of the damage zone being probed by X-rays, we calculated the sample thickness  $x$  required to reduce the amount of transmitted X-ray intensity by half (the so-called half-value layer). The mass absorption coefficients for X-ray Cu cathode radiation in C and Si are  $4.51$  cm<sup>2</sup>/g and  $63.7$  cm<sup>2</sup>/g, respectively, giving  $45.94$  cm<sup>2</sup>/g for SiC [7]. These values give the linear absorption coefficient  $\mu_{SiC} = 147.5$  [cm<sup>-1</sup>] and  $x \approx 15$  μm at  $\omega = 15^\circ$ , and the X-rays thus penetrate both the substrate and the damage zone.

## 2.2 Swelling results by XRD

Figure 2.3 shows  $2\theta$ - $\omega$  scans from C-irradiated 4H-SiC plotted as a function of the scattering angle (the bottom horizontal axis) and the total elastic strain normal to the surface (the top horizontal axis). A spectrum from an un-irradiated sample is shown as a reference. The main sharp Bragg peak of (0004) and intensity – denoted as  $I_0$  – is located at  $2\theta = 35.7^\circ$  and comes from the unperturbed SiC crystal. All spectra exhibit the substrate peak. However, for the irradiated samples this peak becomes broader, which can be especially visible at the lowest temperature of  $600^\circ\text{C}$ . For Kr-irradiation (see Fig. 2.4) the substrate peak is broadened as well, however, to a lesser extent than for the C case.

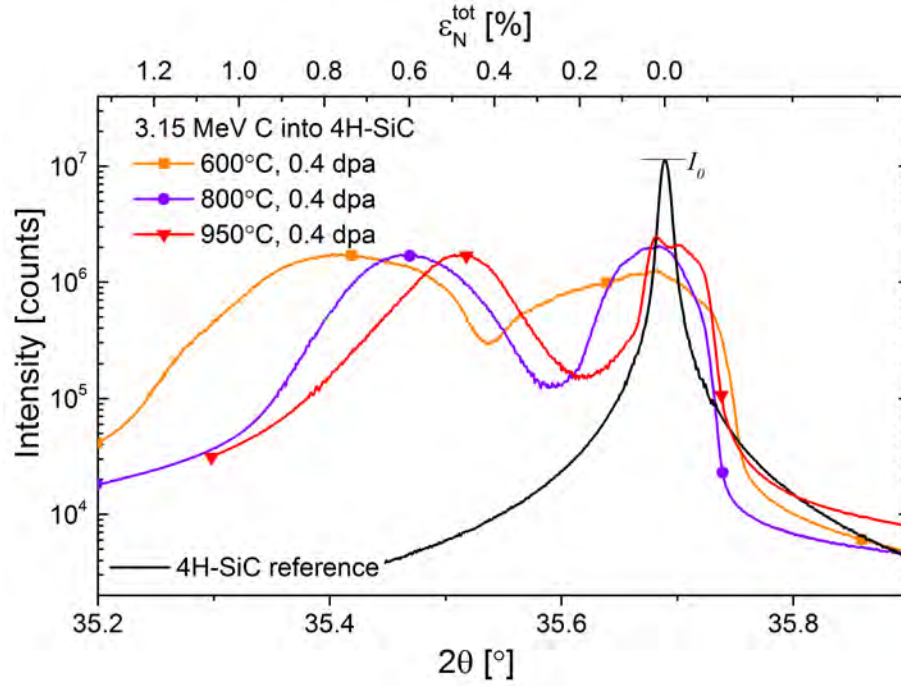


**Figure 2.3** 2 $\theta$ - $\omega$  scans at (0004) pole of 3.15 MeV C-irradiated 4H-SiC up to 0.4 dpa at temperatures between 600 °C and 950 °C. A spectrum from an un-implanted sample is shown for reference. With increasing temperature, the strain decreases.

After irradiation, a new, asymmetric, broad peak on the low-angle side appears (see Fig. 2.3 and Fig. 2.4), coming from the damaged part of the crystal. Within the damage zone, irradiation causes a loss of the long-range order due to accrual of point and black spot defects, which gives rise to elastic strain and swelling. The location of the satellite peak (see Fig. 2.3 and 2.4(a)) provides information on irradiation-induced strain. Position of the satellite peak at  $2\theta < 2\theta_B$  indicates an increase of the interplanar distance, which means that the implanted layer undergoes tensile strain along the direction normal to the surface of the crystal and along the irradiation direction. The lack of fringes is a result of curve broadening due to root-mean-squared (rms) strains. The width of the damage peak is inversely proportional to the width of the damaged zone with the given level strain. Since the satellite peak for C irradiation is broader than for Kr, this indicates that the region with the maximum strain is narrower. As shown in Fig. 2.3, strain builds up with decreasing temperature, which indicates the presence of simple defects (e.g., interstitials and vacancies) and a lack of extended defects, which can induce plastic relaxation. As also seen in Fig. 2.3, the competitive effect of defect creation and annihilation shifts the satellite peak progressively towards higher  $2\theta$  angles with increasing irradiation temperature. However, even a temperature of 950 °C is not sufficient to ensure complete defect recovery.



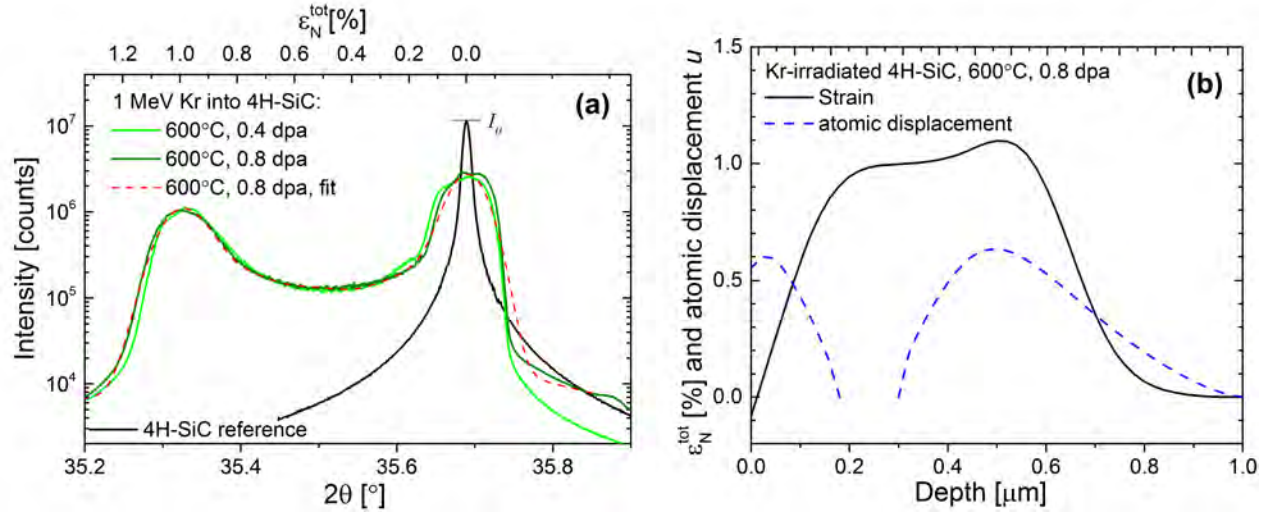


**Figure 2.4** (a)  $2\theta$ - $\omega$  scans at the (0004) pole of 1 MeV Kr-irradiated 4H-SiC at 600 °C up to either 0.4 dpa or 0.8 dpa. A spectrum from an un-implanted sample is shown for reference. No difference in strain is observed above 0.4 dpa; (b) strain and atomic displacement profiles corresponding to 1 MeV Kr-irradiated 4H-SiC at 600 °C up to 0.8 dpa.

### 2.2.1 Total normal strain vs. true normal strain

In the case of the Kr-irradiated 4H-SiC (see Fig. 2.4(a)), estimating the maximum strain is straightforward, as the XRD peaks are fairly sharp, and the intensity of the tail signal from the satellite peak (the region above the tensile strain value of 0.9%) is comparable to the tail intensity for the undamaged sample. The case of C-implanted SiC is more complicated, because the satellite peaks are much broader, and the intensities of the tails of the low-angle satellite peaks are higher than for the undamaged sample, even at strain values above 1.5% (not shown). To estimate the maximum strain, a Gaussian function was fitted to the satellite peaks, and the expected value defined the total in-plane strain  $\epsilon_N^{tot}$ , with the standard deviation as strain error. The obtained  $\epsilon_N^{tot}$  is a measure of the elastic strain produced in a thin layer laterally confined by the unperturbed substrate. This total strain differs from the elastic strain that would be measured in a freestanding solid (e.g., as in the case of neutron-irradiated experiments) and therefore yields only approximate values of swelling [8-11]. To find the true strain in the damaged zone  $\epsilon_N^d$  and separate it from the “substrate strain”  $\epsilon_N^s$  (result of Poisson expansion), we follow the procedure proposed by Debelle and Declémy [12] adjusted to hexagonal <0001>-oriented system, in which the true and the total normal strains are related through the elastic constants as follows,

$$\epsilon_N^{tot} = \epsilon_N^d + \epsilon_N^s \quad \text{Equation 2.2}$$

$$\frac{\varepsilon_N^d}{\varepsilon_N^{tot}} = \frac{C_{11} + C_{12} - C_{13}}{C_{11} + C_{12} + C_{13}} \quad \text{Equation 2.3}$$

Using the elastic constants  $C_{11}$ ,  $C_{12}$ , and  $C_{13}$  for 4H-SiC from Kamitani *et al.* [13], we estimate that the true strain to be 84% of the total normal strain. Both for C- and Kr-irradiation, the strain values decrease with increasing irradiation temperature, indicating defect annealing. At 600 °C, the strain measured in the Kr-irradiated material is about 27% higher than in the C irradiated samples. However, at 800 °C the strain values for both types of ions are comparable. Kr-irradiation above 0.4 dpa at either temperature does not result in an increase of the strain value, suggesting defect saturation.

### 2.2.2 XRD data modeling

Ion-irradiation entails variation of the spacing of the lattice planes as well as atom displacements from their lattice sites. The first ( $\varepsilon_N^{tot}$ ), results in an angular shift of diffracted intensity from that of the unperturbed substrate, while the second (Debye-Waller factor  $M$ ) lowers the structure factor of the damaged region. We attempt to reproduce both phenomena by modeling the spectra of 1 MeV Kr-irradiated 4H-SiC at 600 °C up to 0.8 dpa (see Fig. 2.4(b)) using least-square fitting based on the approach proposed by Boulle and Debelle [14].

The lack of specific features, such as interference fringes, inhibits the possibility of an absolute determination of strain profile. Therefore, SRIM's damage profile was used as an initial condition for the strain profile modeling and its shape was refined until agreement with the experimental data was reached. Fitting was done using a classical least-square algorithm, which is a local search around the starting point. Constraints were placed on the maximum possible value of the strain based on the position of the satellite peak. Both strain and Debye-Waller factor profiles were fitted simultaneously and are independent from each other. The results show that the irradiated and the underlying pristine crystal are heterogeneously strained. Hence, in addition to the strain profile obtained (see Fig.2.4(b)), there also are some random lattice spacing fluctuations, which turn out to be normally distributed with a root-mean-squared strain of approximately 0.056%, which account for the broadening of both the substrate and the damage peak. The strain profile in the damaged sample is almost flat ( $\varepsilon_N^{tot} \approx 0.9\%$ ), which suggests that the sample was implanted above the defect saturation damage level. In Figure 2.4(b), a narrow region in slight compression (i.e., with negative strain) is noticeable close to the surface (< 15 nm). This region accounts for the high intensity at the right-hand side of the un-irradiated Bragg peak. Excluding this region the fitted data results in a purely tensile strain profile. However, since the measured data is heavily broadened, an absolute determination of the strain profile is not possible.

We were not able to obtain a physically meaningful D-W profile, as the measured data does not contain enough information (due to heavy damage) to prevent the parameters from diverging. Specifically, Fig. 2.4(b) shows the atomic displacement  $u$  from the  $d_{004}$  plane (in %, defined as  $u/d_{004}$ ) calculated from the D-W factor, with 0 meaning no displacement and 1 being 100% of displacement (amorphization). One can see a discontinuity in the region between 0.2 and 0.3  $\mu\text{m}$ , with an unphysical ( $> 1$ ) DW factor ( $u/d_{004} < 0$ ), which could indicate a change in the structure or defect clustering.

### 2.3 Discussion of swelling in SiC as measured by XRD

XRD results show that for both C- and Kr-irradiation the increase of irradiation temperature leads to a reduction of tensile strain. A higher damage level (at both 600 °C and 800 °C) in Kr-irradiated samples causes no shift of the satellite peak, which indicates no change in strain and implies defect saturation. At 600 °C and 0.4 dpa, the measured XRD strain is lower in C-irradiated samples. In contrast, at 800 °C and 0.4 dpa, it is the same as for Kr-irradiation (see Fig. 2.5). This observation can be explained by the fact that C is a self-ion and as such can form  $C_{Si}$  anti-site defects, which have a negative formation volume (they decrease strain).

The values of swelling from XRD are compared to the previously published data in Fig. 2.5. The label next to each data point indicates its damage level as calculated according to the procedure mentioned in section 2.1.1. It is evident that the magnitude of swelling decreases with increasing irradiation temperature up to 1100 °C, which is a sign of small defect recovery and lack of defect growth due to its migration. No definite conclusion can be made about the effect of damage level or damage rate (type of irradiation particles) on the magnitude of swelling. However, in general it seems that swelling values derived from the total in-plane strain are higher than from other methods like TEM or linear dimension change, which is mainly due to the fact that the effect of substrate is unaccounted for in the XRD method. In our approach, we subtract the substrate strain from the total strain in the XRD analysis. However, we do not exclude the swelling of the matrix caused by the extraneous interstitials (Kr, C), which can contribute to swelling.

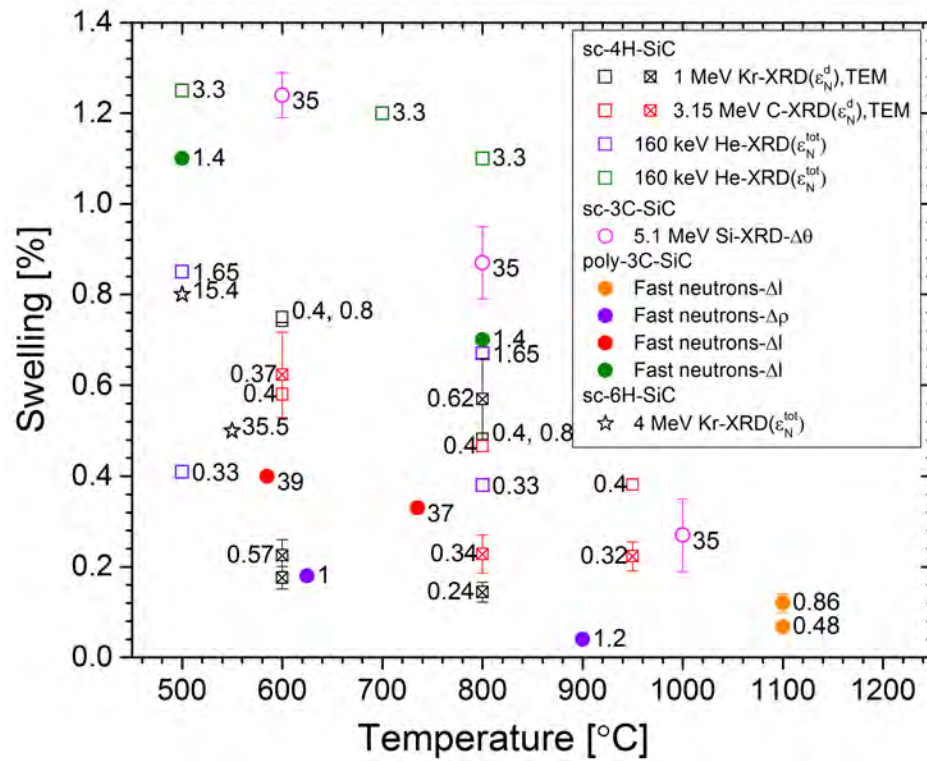


**Figure 2.5** Summary of swelling data measured by various methods ( $\epsilon_N^d$ : true normal strain,  $\epsilon_N^{tot}$ : total normal strain,  $\Delta\theta$ : peak shift,  $\Delta\rho$ : density change,  $\Delta l$ : linear dimension change, and TEM) in neutron- (solid symbols) and ion-irradiated (empty symbols) 4H-SiC (squares), 3C-SiC (circles), and 6H-SiC (stars). The labels indicate the damage levels in dpa of exposed samples. Sources:  $\square\boxtimes$   $\square\boxtimes$ – this work,  $\square$ [8],  $\square$ [9, 11],  $\circ$ [15],  $\bullet$ [16],  $\bullet$ [17],  $\bullet$ [18],  $\bullet$ [19],  $\star$ [12]

## 2.4 Summary of results

The ion-induced swelling of single crystal 4H-SiC was studied by x-ray diffraction (XRD) technique. It was observed that the damage zone underwent tensile strain. The total measured value of the strain is a result of the strain in the damage zone and the “substrate strain”, which is the result of Poisson expansion. The tensile strain profile does not assume the shape of the damage profile calculated by SRIM and is rather quasi-flat throughout the entire damage zone, suggesting defect saturation, which is also confirmed by the lack of change in the swelling values with increasing damage level. True strain, which is 84% of the total strain, reflects the actual swelling of the damage zone. It was observed that as the irradiation temperature increased, the swelling decreased, which is attributed to defect recovery. However, it is possible that XRD overestimates swelling, as it includes the swelling caused by a high fluence of implanted ions (C and Kr).

## 3 Imaging of defects in ion irradiated SiC

We have characterized the size and density of irradiation-induced defects in 4H and 3C-SiC for both ion irradiation and neutron irradiation. These data contribute to and validate the body of data from previous similar measurements.

We have also made an important discovery that conventional diffraction contrast TEM and high-resolution phase-contrast imaging significantly underestimate the density of very small defect clusters, one nanometer or less in diameter. Low-angle dark-field STEM, a high resolution imaging mode that is very sensitive to strain fields, detects a significantly larger density of small defects under various irradiation conditions. These defects make some contribution to irradiation-induced swelling, but more importantly they require significant changes in our physical models of the evolution of the defect population, as captured in the cluster dynamics simulations.

Finally, we have discovered a new irradiation-induced diffusion mechanism for entire defect clusters by observing their motion under the intense electron beam of a high-resolution STEM. This is also new physics that contributes to the evolution of the cluster size distribution during irradiation.

### 3.1 Conventional TEM characterization of ion- and neutron-irradiated SiC

Figure 3.1 shows conventional bright field, diffraction-contrast TEM images of 3C-SiC irradiated at 800°C to (a) 0.54 dpa with krypton ions, (b) 0.48 dpa with carbon ions and (c) 30 dpa with neutrons. A large fraction of irradiation-induced structural features are black spot defects or small clusters, which show strain contrast in TEM images. The BSDs are mostly circular or oval in shape. These images mimic the acquisition conditions widely used in the literature and produce similar results for the BSD size and density as a function of irradiation conditions.

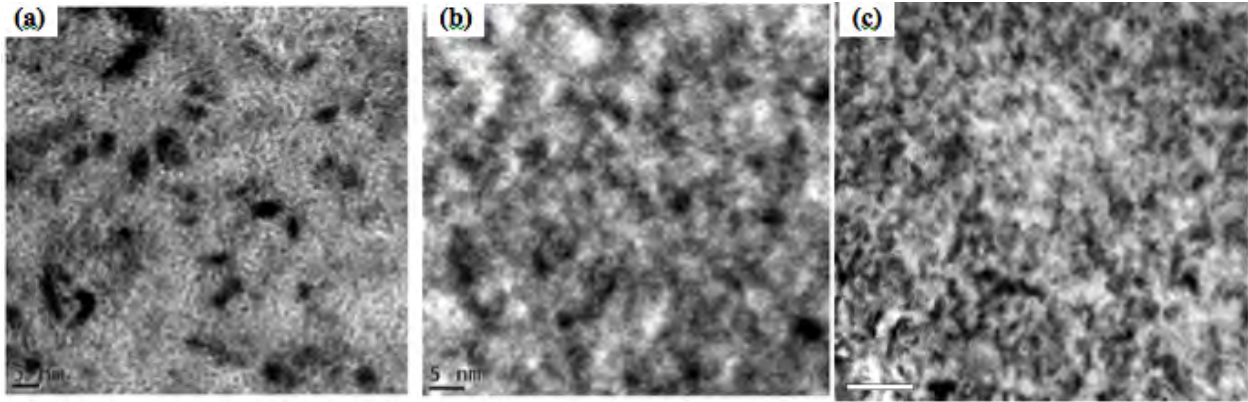


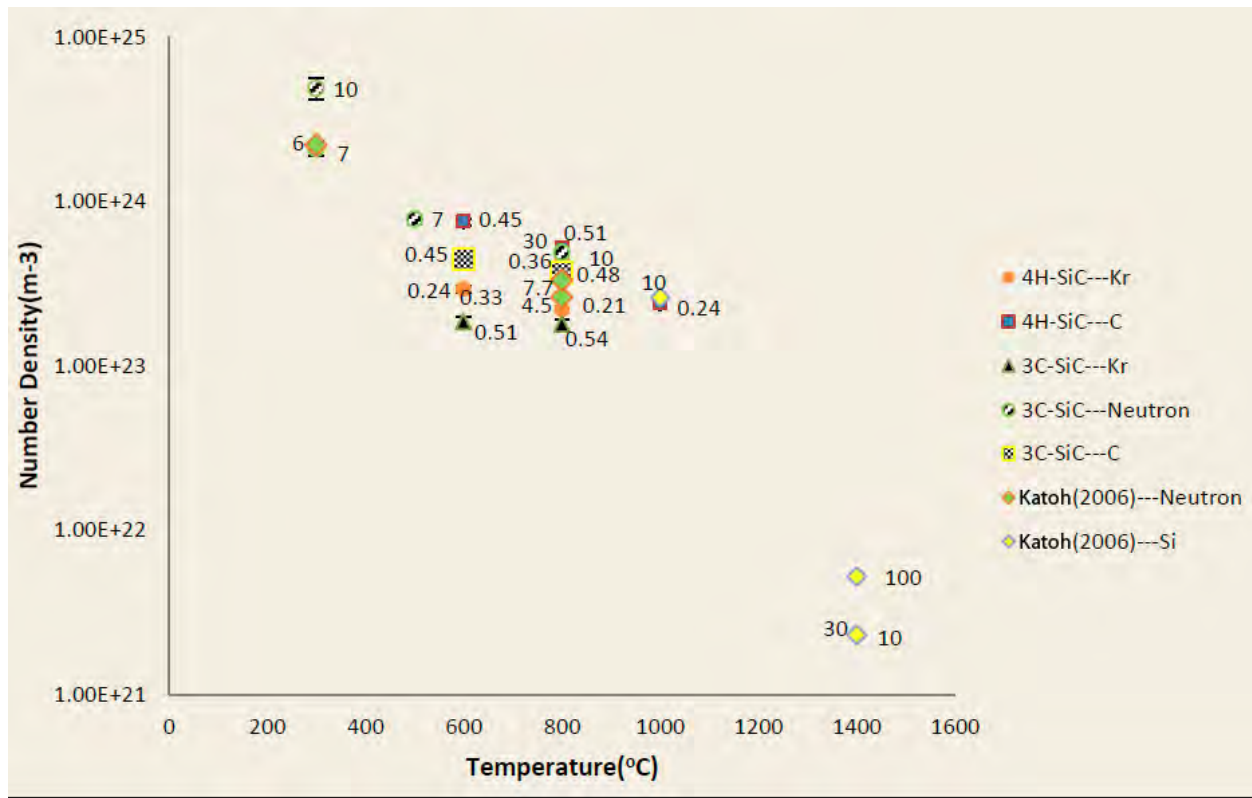
**Figure 3.1** Bright field TEM images of BSDs in krypton-, carbon- and neutron-irradiated 3C-SiC at 800°C, shown in (a), (b) and (c), respectively.

**Table 3.1** TEM results summary of BSDs

Samples	Implanted particles	Irradiation Temperature (°C)	Fluence (dpa)	Size(nm)	Density ( $\times 10^{23} \text{ m}^{-3}$ )
4H-SiC	Kr	600	0.24	$1.1 \pm 0.1$	$2.9 \pm 0.1$
		800	0.21	$1.3 \pm 0.1$	$2.2 \pm 0.1$
		600	0.33	$1.3 \pm 0.1$	$4.2 \pm 0.2$
		800	0.36	$1.4 \pm 0.1$	$4.3 \pm 0.3$
	C	600	0.45	$1.4 \pm 0.1$	$7.5 \pm 0.4$
		800	0.51	$1.7 \pm 0.1$	$5.2 \pm 0.3$
		1000	0.24	$1.6 \pm 0.1$	$2.4 \pm 0.1$
3C-SiC	Kr	600	0.51	$1.8 \pm 0.1$	$1.9 \pm 0.1$

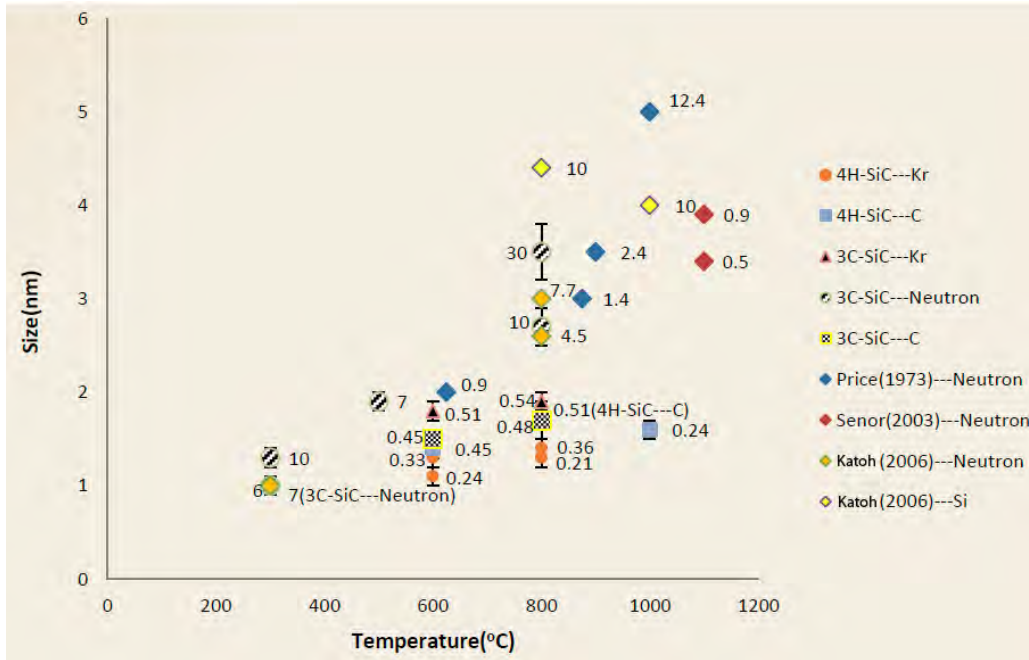
		800	0.54	$1.9 \pm 0.1$	$1.8 \pm 0.1$
	Neutron	300	7	$1.0 \pm 0.1$	$21 \pm 2$
		500	7	$1.9 \pm 0.1$	$7.8 \pm 0.5$
		300	10	$1.3 \pm 0.1$	$49 \pm 7$
		800	10	$2.7 \pm 0.2$	$3.8 \pm 0.3$
		800	30	$3.5 \pm 0.3$	$4.9 \pm 0.4$
	C	600	0.45	$1.5 \pm 0.1$	$4.5 \pm 0.3$
		800	0.48	$1.7 \pm 0.2$	$3.7 \pm 0.4$

Table 3.1 summarizes all the TEM data of this type on ion-and neutron- irradiated 4H- and 3C-SiC. The mean diameters of the ion-irradiated samples are mostly between 1 nm and 2 nm, and the volume number densities are  $\sim 10^{23} \text{ m}^{-3}$ . For the samples irradiated with neutrons at high irradiation temperature and dose (800 °C, 10 dpa and 30 dpa), the average sizes over 2 nm, perhaps due to a larger fraction of small dislocation loops. Sample irradiated with neutrons at low temperature yield very high defect densities in the  $10^{24} \text{ m}^{-3}$  range.



**Figure 3.2** BSD number density vs temperature. Katoh (2006) corresponds to Ref. [20].





**Figure 3.3** BSD size vs temperature. Katoh (2006) corresponds to Ref. [20]. Price (1973) corresponds to Ref. [17].

Figure 3.2 and Figure 3.3, respectively, show the irradiation temperature and dose dependence of defect cluster sizes and number densities. The number beside each data point is its irradiation dose. The sizes of the defects grow modestly in the range of 1-2 nm, except for 3C-SiC irradiated at 800 °C with 10 dpa and 30 dpa, while the number density of defects varies more significantly. The sizes of defects clusters increase with elevated irradiation temperatures and dose. The densities decrease with temperature, while increasing with irradiation dose.

Overall, these data agree with previous values in the literature in both absolute value and trend. Their value is in extending the range of LWR-relevant conditions under, which SiC has been studied and providing baseline data for our other defect density characterization methods, which makes them more useful to the community.

In the ion-irradiated specimens reported in Table 3.1, BSDs were the primary defect. A large fraction of small dislocation loops were observed in the neutron-irradiated samples at 300 °C, 10 dpa and 30 dpa, as shown in Fig. 3.4. These weak beam dark field images were taken from the same area in two different two beam conditions near  $\mathbf{B} \sim [110]$  with  $\mathbf{g} = (11-1)$  and  $(200)$  reflections, respectively. The loops marked in squares show strong contrast with  $\mathbf{g} = (11-1)$ , but with  $\mathbf{g} = (200)$ ; the loops in circles are strongly visible with  $\mathbf{g} = (200)$ , but invisible with  $\mathbf{g} = (11-1)$ . The triangles identify the features existing in both images as perhaps BSDs or perhaps small loops parallel to other planes. These loops were not seen in the neutron-irradiated 3C-SiC at 300 °C and 7 dpa, and there were relatively sparse loops for samples at 500



°C and 7 dpa. Thus, it appears that with an increase of neutron irradiation fluence and temperature, BSDs tend to grow into loops. Other kinds of irradiation-produced defects, such as voids, cavities or dislocation networks, were not found in any of the ion- and neutron- irradiated samples.

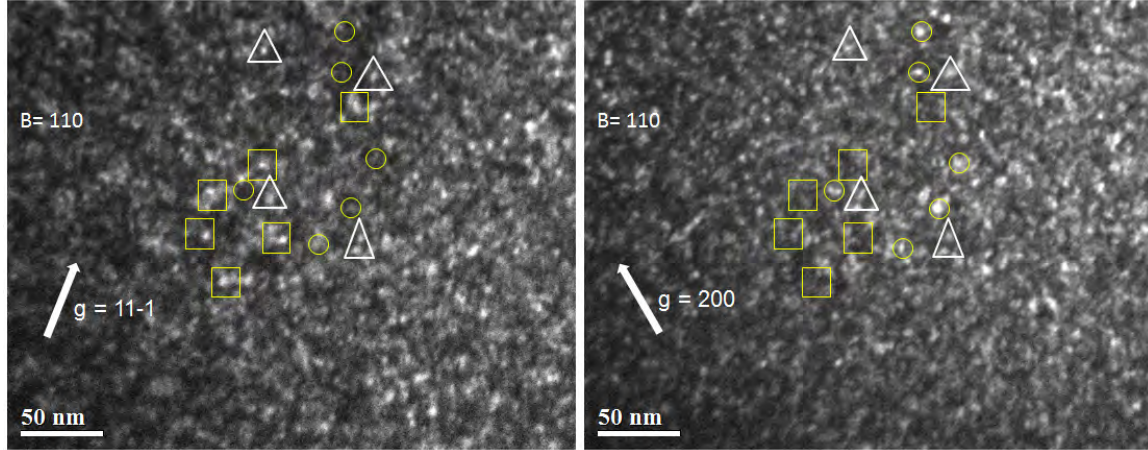


**Figure 3.4** Weak beam dark field images of mixture of BSDs and small dislocation loops in 3C-SiC irradiated at 800 °C and 10 dpa.

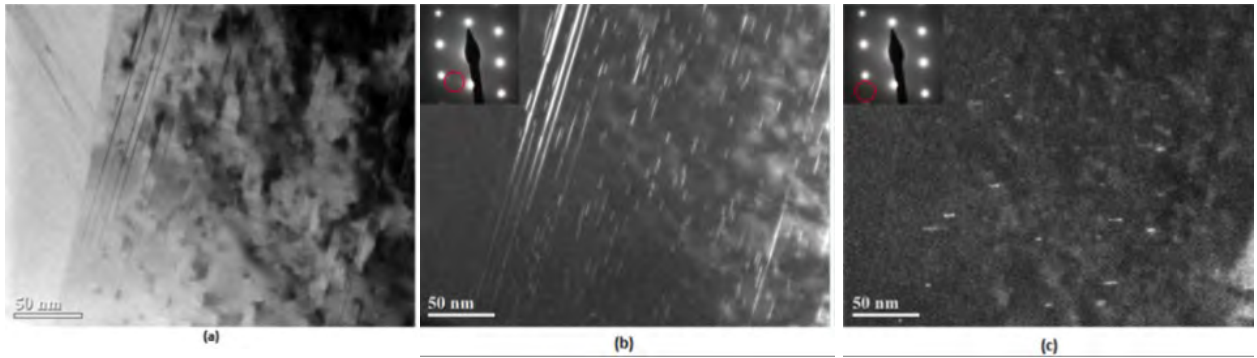


**Figure 3.5** (a) Bright-field image of 3C-SiC after neutron-irradiated samples at 800 °C and 30 dpa; (b) (c) Dark-field image of Faulted loops taken using streaks in the diffraction pattern.

Frank faulted loops were detected only in neutron-irradiated samples at 800 °C and 30 dpa. Figure 3.5(a) shows the bright-field image of edge-on faulted loops in 3C-SiC; (b) and (c) are weak beam dark field images taken from the same area with the beam direction  $\mathbf{B}$  near a  $[110]$  zone axis. (a) is visualized from  $[11\bar{1}]$  satellite streak, and (b) is taken from  $[200]$  satellite streak. Apparently, most of the Frank loops preferentially occupy  $\{111\}$  planes, except for stacking faults that exist in the as-synthesized 3C-

SiC, while only a very few are on  $\{200\}$  planes. In the electron diffraction patterns for other neutron-irradiated SiC at 300 °C - 800 °C and below 10 dpa, no rel-rod streaks were detected.

### 3.2 LAADF STEM characterization of ion-irradiated SiC

Figure 3.6 shows example low-angle annular dark field (LAADF) STEM images of black-spot defects in 4H-SiC irradiated under a variety of conditions. The strain contrast in the image was emphasized by decreasing the STEM convergence angle to 17.5 mrad from the usual value of 24.5 mrad and using lower a detector collection than the 50 to 250 mrad normally used in STEM imaging to produce Z-contrast images.. The periodic bright spots are Si atomic columns. Carbon columns are not visible in this imaging mode because they scatter electron more weakly than Si. Some patches of the atomic lattice are darker than others. Those are BSDs, visible due to their strain field. The identification of these image features as BSDs is confirmed by Z-contrast images of the same area, which show no dark patches, and control LAADF images of an unirradiated part of the same TEM sample. Similar BSD contrast is also obtained in LAADF STEM images of ion irradiated 3C-SiC.

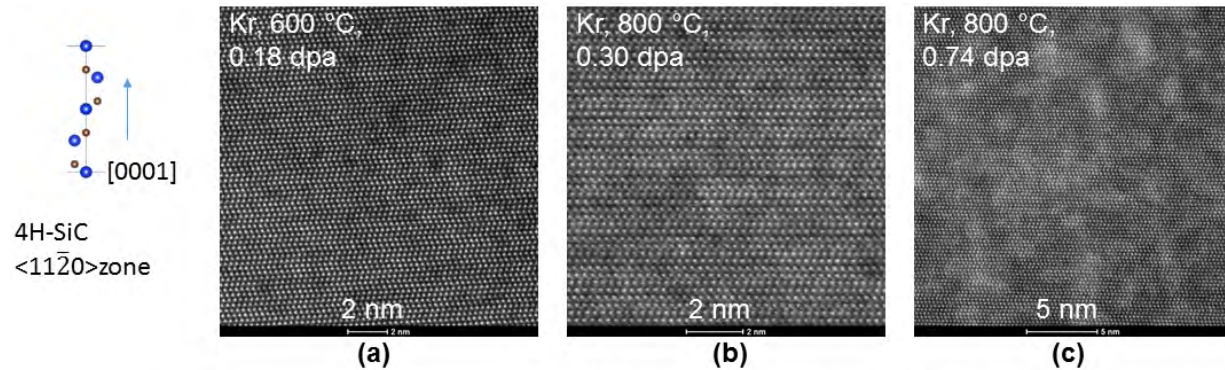


**Figure 3.6** LAADF-STEM images of BSDs and defect clusters in Kr and C-irradiated 4H-SiC, imaged with a 17.5 mrad semi-convergence electron probe and low collection angle. (a) 1 MeV Kr irradiation at 600 °C, 0.18 dpa. (b) Kr irradiation at 800 °C, 0.30 dpa, (c) Kr irradiation at 800 °C, 0.74 dpa.

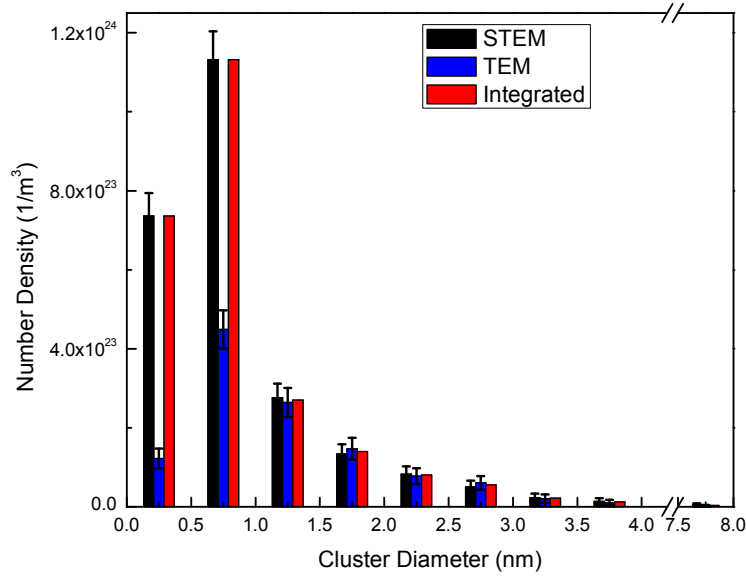


**Figure 3.7** Size distribution of STEM results and TEM results of Kr-irradiated 3C-SiC at 800 °C and 0.36. Integrated distribution is a combined TEM and STEM distribution that is used when comparing to cluster dynamics simulations.

Figure 3.7 shows the size distribution of krypton-irradiated 3C-SiC. Characterizing defect size distributions using high resolution imaging is fairly labor-intensive. The data set contains 543 data points from 21 images taken in the same conditions and nearby areas in specimen. The diameters are in a range of about 0.4 nm to 8.3 nm, and a large fraction (~74.2%) of the defects have diameters smaller than 1 nm. The number densities present a decreasing trend with increasing sizes from 1 nm.

TEM results on the same sample and depth along the implantation profile are also presented to Fig. 3.7 for comparison. Both STEM and TEM results reveal the sizes are mostly between 0.5nm and 1nm. The sizes distributions from TEM results are in good agreement with STEM results for diameters greater than 1 nm. But for those smaller than 1 nm, the densities from STEM imaging are approximately 1.5 times more than those from TEM results. These results indicate that TEM imaging significantly underestimates the densities of BSDs smaller than 1 nm.

#### 4 Defect modeling

This section consists of four parts. In Section 4.1, we introduce the cluster dynamics (CD) framework used in this study. In Section 4.2 we discuss predictions of the model based on known parameters for SiC. We demonstrate that with the currently known physics of irradiation-induced defects in SiC, it is not possible to reproduce experimental distribution of cluster sizes. In Section 4.3 we discuss potential new physics that needs to be included in the model and we present predictions of the model with this new physics included. We specifically demonstrate what physics is necessary to include in order to match

experimental data. Finally, in Section 4.4 we provide predictions of swelling from our model and we compare the results to experimentally measured swelling for SiC samples irradiated by 1 MeV Kr<sup>+</sup> at 800 °C.

#### 4.1 Cluster dynamics (CD) method

In a mean-field CD method the evolution of density  $C_n$  of cluster of size  $n$  is described by the following equation [21, 22]

$$\frac{dC_n}{dt} = P_n + \sum J_{n-m \rightarrow n} - \sum J_{n \rightarrow n-m} + Q_n \quad \text{Equation 4.1}$$

where  $P_n$  is the production rate of clusters, which comes from external factors, such as irradiation.  $J_{n-m \rightarrow n}$  and  $J_{n \rightarrow n+m}$  are the net fluxes describing cluster growth,  $Q_n$  is the reaction rate of cluster  $n$  with all other kinds of reactants except clusters and components, such as surfaces, grain boundaries, etc. Here, we have solved equation 4.1 (for each cluster size) using Suite of Nonlinear and Differential/Algebraic equations Solvers (SUNDIALS), a powerful ODE solver developed by Lawrence Livermore National Laboratory (LLNL).

#### 4.2 CD model with known physical parameters for SiC

##### 4.2.1 Formulation and assumptions of the model

Our CD model relies on the following assumptions:

1. Migration energies of point defects and the barrier to their recombination reactions are taken from Ref. [23]. Point defects included in our model are: carbon interstitial ( $C_I$ ), silicon interstitial ( $Si_I$ ), carbon vacancy ( $V_C$ ), silicon vacancy ( $V_{Si}$ ), carbon antisite ( $C_{Si}$ ), where C occupies Si lattice site, and Si antisite ( $Si_C$ ). We also include the possibility of forming a metastable defect complex  $V_C - C_{Si}$ , which was firstly identified by Bockstedte *et al.* [24].
2. There are no vacancy clusters included in our model, which is also consistent with previous studies that showed void swelling starts from 1100 °C– 1250 °C [20].
3. Clusters can only formed by absorbing and emitting interstitials since cluster are assumed to be immobile due to their high migration barriers.

Under the above assumptions, master equations that govern evolution of defects in our system can be written as

for clusters: 
$$\frac{dC_n}{dt} = J_{n-1 \rightarrow n} - J_{n \rightarrow n+1} \quad \text{Equation 4.2}$$

for  $C_I$ : 
$$\frac{dC_{C_I}}{dt} = P_{C_I} - 2 \cdot x_{C_I} \cdot J_{1 \rightarrow 2} - \sum_{n \geq 2} x_{C_I} \cdot J_{n \rightarrow n+1} + Q_{C_I} \quad \text{Equation 4.3}$$

for  $Si_I$ :

$$\frac{dC_{Si_I}}{dt} = P_{Si_I} - 2 \cdot x_{Si_I} \cdot J_{1 \rightarrow 2} - \sum_{n \geq 2} x_{Si_I} \cdot J_{n \rightarrow n+1} + Q_{Si_I} \quad \text{Equation 4.4}$$

for other point defects(OPDs)

$$\frac{dC_{OPD}}{dt} = P_{OPD} + Q_{OPD} \quad \text{Equation 4.5}$$

where  $x_{C_I}$  and  $x_{Si_I}$  represent the fraction of  $C_I$  and  $Si_I$  in a cluster. Here these variables equal 50%, because of our stoichiometric assumption.  $P_{C_I}$  is the production rate of  $C_I$  by irradiation,  $Q_{C_I}$  represents the atomic fraction-changing rate due to reaction rate among point defects. The net flux among adjacent clusters is

$$J_{n \rightarrow n+1} = \beta_{n,n+1} C_n - \alpha_{n+1} C_{n+1} \quad \text{Equation 4.6}$$

where  $\beta_{n,n+1}$  is the absorption rate of an interstitial by cluster  $n$  and it is defined as

$$\beta_{n,n+1} = 2\pi(r_n + r_1)D_{\text{eff}}^d/\Omega \quad \text{Equation 4.7}$$

$\Omega$  is the average atomic volume in 3C-SiC,  $r_n$  is the radius of the planar clusters with Burgers vector  $b = [111]$ .  $D_{\text{eff}}^d$  is the effective diffusion coefficient of monomers that can be absorbed by cluster  $n$ . The effective diffusion coefficient definition in multi-component system by Slezov [25]:

$$D_{\text{eff}}^d = \left( \frac{x_{C_I}^2}{C_{C_I} D_{C_I}} + \frac{x_{Si_I}^2}{C_{Si_I} D_{Si_I}} \right)^{-1} \quad \text{Equation 4.8}$$

where  $D_{C_I}$  and  $D_{Si_I}$  are the diffusion coefficient of  $C_I$  and  $Si_I$ .

Assuming a dilute concentration of interstitials in 3C-SiC, the real time equilibrium cluster distribution can be derived from the classical nucleation theory as

$$\bar{C}_n = \exp\left(-\frac{\Delta G_n}{kT}\right) \quad \text{Equation 4.8}$$

Then, the emission rate of an interstitial from a cluster follows

$$\alpha_{n+1} = \beta_{n,n+1} \frac{\bar{C}_n}{\bar{C}_{n+1}} = \beta_{n,n+1} \cdot \exp\left(-\frac{\Delta G_n - \Delta G_{n+1}}{kT}\right) \quad \text{Equation 4.9}$$

Finally, the production rate of point defects is given by

$$P_{PD} = \Gamma \eta \xi_{PD} \quad \text{Equation 4.10}$$

where  $\eta$  is cascade efficiency and  $\Gamma$  is the dose rate in dpa/s. SRIM calculation based on our 1 MeV  $Kr^+$  irradiation experiments gives  $\Gamma = 2.0 \times 10^{-3}$  dpa/s.  $\xi_{PD}$  is the fraction of a given type of point defect (PD) produced during irradiation. It is calculated from MD simulations of displacement cascade by Swaminathan *et al.* [23].

#### 4.2.2 Parameters of the model

##### Formation energies

Formation energies of point defects in SiC are generally known and can be found for instance in Ref. [23]. For defect clusters we considered formation energies calculated quantum mechanically based on the density functional theory (DFT) by Jiang *et al.* [26] and based on empirical potentials by Watanabe *et al.* [27]. While DFT is a more accurate method, it is limited to a small cluster sizes. The summary of formation energies of clusters as a function of their size is shown in Fig. 4.1. Since energies predicted by DFT and empirical potentials are shifted with respect to each other, we used a number of schemes to combine these two approaches. They include “switching function” and “shifting”. Both of these approaches are illustrated in Fig. 4.1

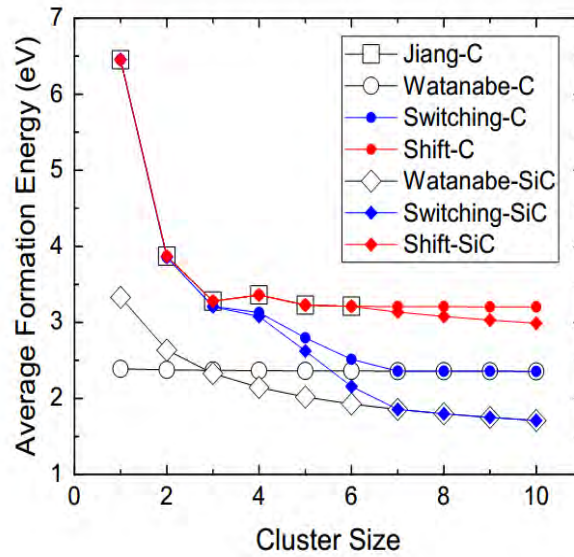


**Figure 4.1** Cluster formation energies of carbon and stoichiometric clusters. DFT data is taken from Jiang *et al* [26], empirical potential data is taken from Watanabe *et al* [27].

##### Cascade efficiency

Cascade efficiency,  $\eta$  depends on incident atom species and energy, direction, and matrix material composition and structure [28]. In the last thirty years various values for  $\eta$  have been reported from experiments and simulations. This range of values is shown in Fig. 4.2 and in our model we will treat  $\eta$  as a parameter fitted within a range of the previously observed values (0.001 to 1).

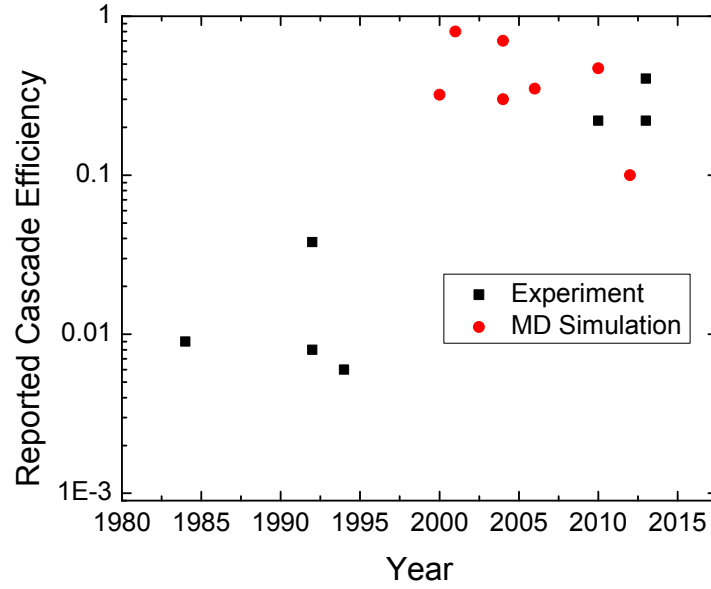


**Figure 4.2** Cascade efficiencies from Refs. [29-42]. Red circles and black squares correspond to simulation and experimental results, respectively.

#### 4.2.3 Results

Cascade efficiency in our simulations was chosen by minimizing the root mean square deviation (RMSD) defined as

$$RMSD = \left( \frac{1}{5} \sum_{i=1}^5 (C_i^{Sim} - C_i^{Exp})^2 \right)^{0.5} \quad \text{Equation 4.11}$$

$C_i^{sim}$  and  $C_i^{exp}$ , respectively, represent simulation and experimental concentration of clusters with  $i$  defects. Only clusters with diameters equal or smaller than 2.5 nm are taken into account (corresponding to the first 5 columns in Fig. 4.3). Interestingly, the results are not strongly dependent on the specific functional form of cluster formation energy vs cluster size (Fig. 4.1). Therefore in our results we picked one method that involves the switching function.

The best fit (lowest RMSD) to experimental data yields  $\eta = 0.007$  (based on the RMSD data and on comparison of the total number of interstitials trapped in clusters observed in STEM experiments and in simulations). This value of  $\eta$  is on the very low end of the range of cascade efficiencies seen previously in SiC. However, even for such low efficiency, there is a significant discrepancy between simulation and experimental data (see Fig. 4.3) and increasing  $\eta$  makes the deviation from experiments larger.

The data in Fig. 4.3 shows that in the current version of the CD model (which includes known physics for irradiated SiC) the cluster nucleation phase is too short and the growth of clusters is too fast compared



to experiments. In subsequent sections we will explore what potential physics can alter this behavior and bring a better agreement with experiment.

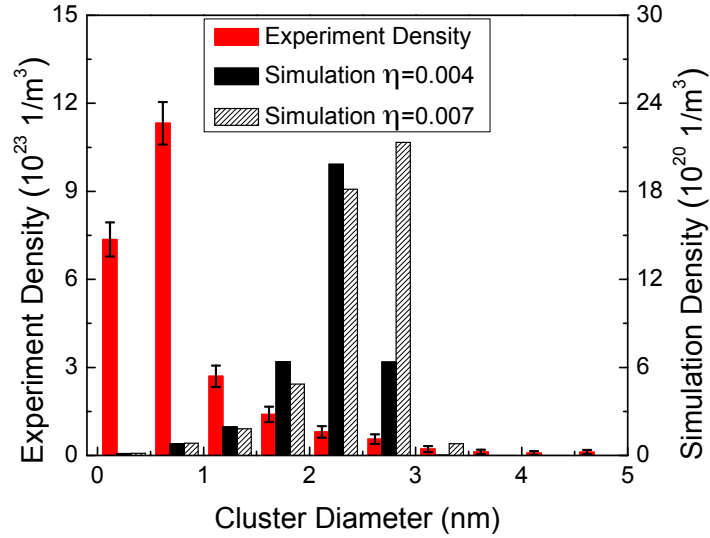


**Figure 4.3** Simulation results with different cascade efficiencies. Red color corresponds to experimental values.

### 4.3 Effects of new physical phenomena in irradiated SiC on predictions of the CD model

#### 4.3.1 Physical phenomena that may be present in irradiated SiC

##### Intra-cascade cluster production

It is possible that some of the clusters form directly in the cascade, instead of arising from interaction of point defects in the cascade settling stage. This phenomenon was found to be necessary to be included in CD models of irradiated tungsten, molybdenum, and iron in order to reproduce experimental cluster distributions [43-46]. Since there is currently no model predicting the size distribution of clusters produced in the cascade as a function of the PKA energy, we adopted the functional form for such distribution from Xu *et al.* [43] and we scaled the function to match the total production of C and Si interstitials produced in SiC, according to Swaminathan *et al.* [47].

##### Cluster mobility

We have recently discovered using accelerated MD simulations that although defect clusters in SiC have inherently high energy barriers ( $> 4 \text{ eV}$ ) and therefore they are expected to be immobile up to 1,200K, these clusters may become mobile under radiation. The dependence of migration energy barrier on cluster size is unknown in SiC and therefore here we adopt an approximation proposed by Xu *et al.* [43]. In this method, pre-factor decrease as a power law with increasing cluster size while migration



barriers are constant when size is smaller than 10 and larger than 20, and increase linearly when the size is between 10-20.

#### Cluster morphology

Although larger black spot defects and dislocation loops (as observed in TEM) have been shown to be mainly planar in irradiated SiC [3, 20, 48], very small clusters can be non-planar [20, 49]. This assertion has been verified by atomistic simulations of Jiang *et al.* [26, 50]. Our inspection of STEM images reveals that on the average approximately 59 % of cluster smaller than 1nm lie within the  $\{111\}$  planes, and among clusters larger than 1 nm about 82% of cluster lie within the  $\{111\}$  planes with  $\pm 30^\circ$  angle error bar. These results show that during irradiation and cluster evolution, there is a non-negligible fraction of clusters that do not lie on the  $\{111\}$  planes. These out-of-plane clusters likely have different properties than the in-plane clusters. Since larger clusters and loops are observed mainly to be in-plane therefore we assume here that the out-of-plane clusters do not grow. Since these clusters are still observed in our sample, we assume that they do not dissolve or annihilate with vacancies (because of high vacancy migration barriers in SiC). Again, the functional form for production of out-of-plane clusters is not available, and here we assume a common power law function and treat the parameters of the function as adjustable in our model.

#### 4.3.2 *Results of the adjusted model*

In Fig. 4.3 we have shown that CD model that includes known physical phenomena for irradiated SiC underestimates cluster production for very small clusters. One possible way to increase concentration of small clusters would be to increase concentration of point defects (by increasing cascade efficiency), which then can accumulate and nucleate many small clusters. However increasing cascade efficiency does not yield results consistent with experiments (see Fig. 4.3) because it leads not only to faster nucleation, but also to faster cluster growth. In fact increasing cascade efficiency makes the already poor agreement between simulations and experiments even worse. Following other authors' approach to increasing concentration of small clusters (see Section 4.3.1 for discussion), we have introduced intra-cascade cluster production in our model. However, we found that introducing intra-cascade cluster production alone does not lead to a reasonable agreement with experiments. As shown in Fig. 4.4, although the concentration of small clusters increased, the growth of clusters has been significantly suppressed because most of the point defects are trapped as small clusters and the driving force to cluster growth is significantly reduced.

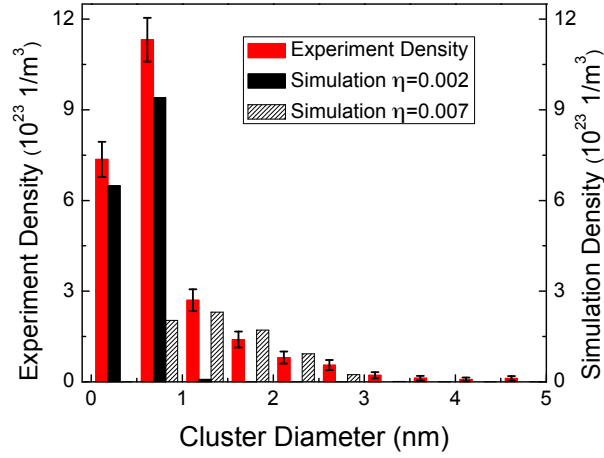


**Figure 4.4** Comparison of experiment and simulation of CD model that includes intra-cascade cluster production.

We have next introduced mobility of in-plane clusters formed during irradiation (while keeping the out-of-plane clusters immobile and unable to grow). Since mobility of small clusters enables their coalescence, this process allows for growth of a certain fraction of clusters. With this phenomenon included in our model, it is now possible to reproduce experimental STEM data (Fig. 4.5).

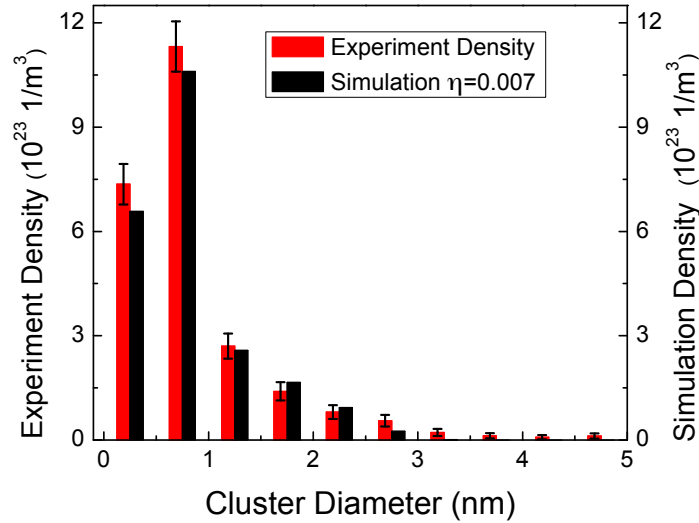


**Figure 4.5** Comparison of results from STEM experiment and CD simulations that include intra-cascade cluster production, mobile cluster and out-of-plane cluster production.

Although inclusion of intra-cascade cluster production, mobile clusters and out-of-plane cluster production is speculative, there is some evidence that these phenomena can be present in irradiated SiC.

In addition our simulations demonstrate that with the current understanding of fundamental radiation effects in SiC, it is not possible to reproduce experimental cluster distribution in this material. Our results provide new insights into what other defect-related phenomena may be active and what is their role on defect evolution in irradiated SiC.

## 5 Characterization of neutron irradiated SiC

### 5.1 Evaluation of neutron irradiation creep

Irradiation experiment and evaluation of irradiation creep strain was conducted under support by Office of Fusion Energy Sciences, U.S. Department of Energy and US–Japan TITAN Collaboration on Fusion Blanket Technology and Materials. The additional microstructural analysis in Section 5.2 is conducted in this project. The material used was high purity monolithic CVD SiC produced by Rohm & Haas (currently Dow Chemical Co., Marlborough, Massachusetts). Specimens were annealed in a flowing argon environment at 1900°C for 1 h before machining to remove the pre-existing defects such as stacking faults. Irradiation creep behavior was investigated by using bend stress relaxation (BSR) tests. Initial applied flexural stress was up to ~300 MPa. Details of test procedure and method to evaluate creep strain can be found elsewhere [51, 52]. Neutron irradiation was conducted at the High-Flux Isotope Reactor (HFIR). The specimens were irradiated at ~400–500 °C up to 31 dpa-SiC (1 dpa =  $1.0 \times 10^{25}$  n/m<sup>2</sup> ( $E > 0.1$  MeV) is assumed). The damage rate was  $\sim 1 \times 10^{-6}$  dpa/s.

Creep coefficient, which is normalized creep strain with respect to stress and neutron fluence is used to be an indication of creep rate [51]. The instantaneous creep coefficient ( $K$ ) is defined by:

$$K \cong \frac{\varepsilon_2 - \varepsilon_1}{\sigma(\gamma_2 - \gamma_1)} \quad \text{Equation 5.1}$$

where  $\gamma_1$  and  $\gamma_2$  ( $\gamma_1 < \gamma_2$ ) are neutron fluences,  $\sigma$  is average stress during irradiation, and  $\varepsilon_1$  and  $\varepsilon_2$  are irradiation creep strains following irradiation at a fluence of  $\gamma_1$  and  $\gamma_2$ , respectively. The coefficient divided by stress is reasonable because liner relationship between applied stress level and creep strain was confirmed in this study and also in previous work [51]. The creep strain was obtained from BSR tests. Figure 5.1 shows fluence dependence of the instantaneous creep coefficient of CVD SiC. The highest and lowest horizontal error bars indicate the fluence of  $\gamma_1$  and  $\gamma_2$  for each data point, respectively. The vertical error bars show one standard deviations. The creep coefficients for low dose were obtained in our previous study [51]. The creep coefficient rapidly decreases with increasing fluence up to ~1 dpa, and then the creep coefficients appeared to be constant of  $\sim 1 \times 10^{-7}$  [MPa<sup>-1</sup> dpa<sup>-1</sup>] at 380 to 540 °C. Figure 5.1 also shows creep behavior based on models such as swelling-creep coupling[51] and secondary creep with constant creep coefficient. The swelling coupling creep is explained with anisotropic swelling due to anisotropic SIA defects formation under applied stress. The important findings from Fig. 5.1 are: 1) irradiation creep operates in SiC up to 30 dpa; 2) the creep behavior is described with simultaneous

transient creep of swelling-creep coupling model and secondary creep; and 3) the creep rate is very slow above 1 dpa. The creep mechanism will be discussed based on microstructural evolution.

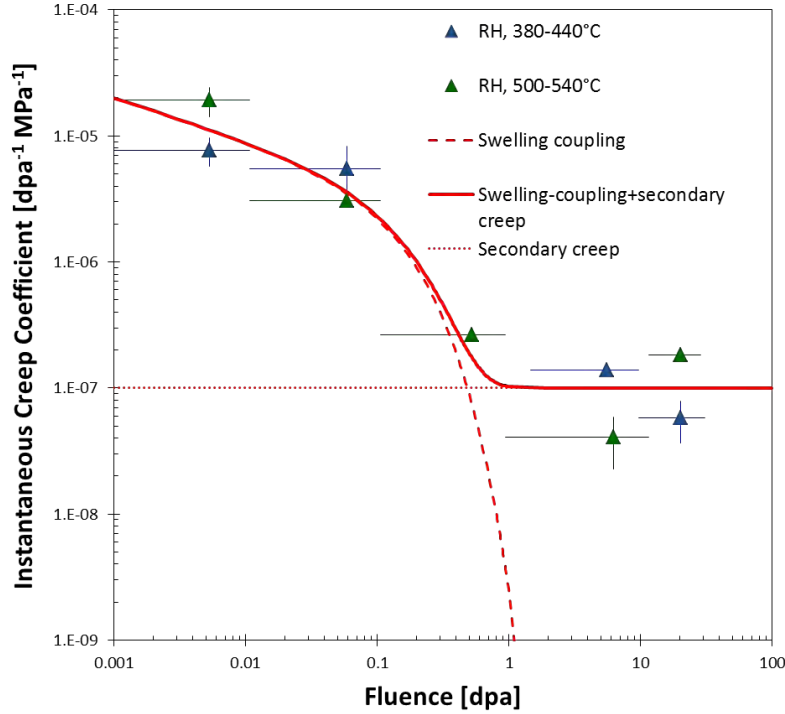


**Figure 5.1** Neutron fluence dependence of instantaneous creep coefficients of CVD SiC materials [20].

## 5.2 Microstructural evolution under irradiation with applied stress

Microstructures of irradiated SiC material were investigated using TEM. The TEM foils were taken from uniaxially tensile-stressed area of the creep specimens. Details of the specimen fabrication procedure are described in elsewhere [53]. The specimen was prepared using a Fischione model 1010 argon ion-milling operated at 3–5 keV. Irradiation defects were observed using a Philips Tecnai 20 operated at 200 kV.

Observed microstructural defects were small clusters, loops, stacking faults, and grain boundaries. The stacking faults and grain boundaries were originally exist in the material. No obvious change in these pre-existing defects was confirmed. Figure 5.2 shows TEM dark field images with small defect clusters in the creep specimen irradiated at 500 °C to 11.6 dpa. The two micrographs were taken from similar location, but taken using different  $g$  vector. One  $g$  vector is near parallel to the stress axis, and the other is near perpendicular to the stress axis. Average defect size and the number density are  $\sim 3$  nm and  $\sim 1 \times 10^{23} \text{ m}^{-3}$ , respectively, in both images. The point to evaluate microstructure of creep specimen is investigation

of anisotropy of defect formation due to applied stress. However, the anisotropy was not identified for the small defect clusters in dark field images with various different  $g$  vectors in this study.

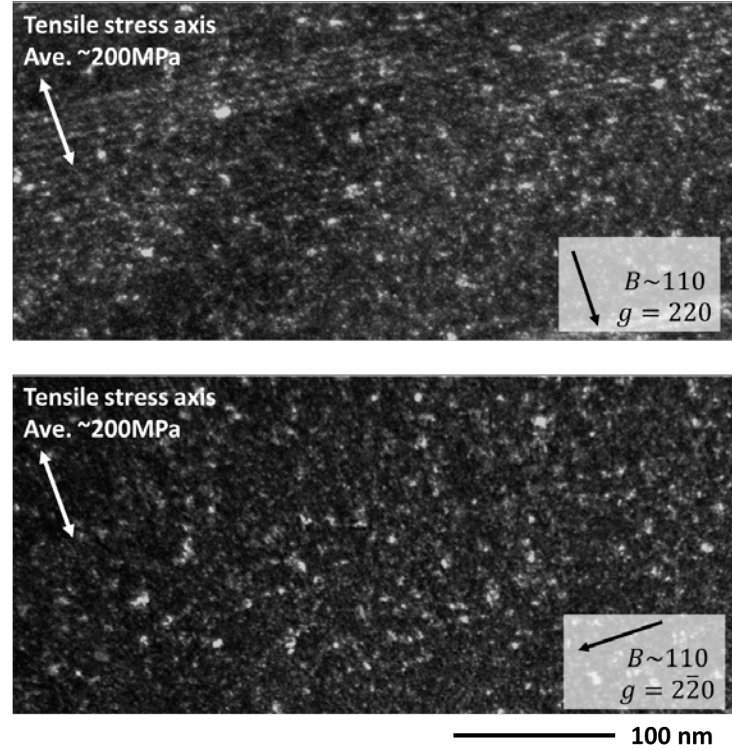


**Figure 5.2** Weak beam dark field images of CVD SiC specimen irradiated at 500 °C to 11.6 dpa with applied stress. The imaging conditions and tensile stress axis are indicated in micrographs.

Dislocation loops in the creep specimens were selectively observed by using dark field imaging with streak to evaluate anisotropy of loop formation. The habit plane is  $\{111\}$  family of planes. The edge-on loops were taken from  $[110]$  direction as shown in Fig. 5.2. A pair of streak images for certain irradiation condition was taken from identical area, but taken using different streak indicated in the diffraction pattern. Line shape of the loop was adjusted to lie near perpendicular or parallel to the stress axis in the micrographs. The former loop lies on stressed  $\{111\}$  planes and the latter lies on non-stressed or less stressed  $\{111\}$  planes. Following irradiation at 500 °C to 11.6 dpa, the loops with very small number density were observed mostly perpendicular to tensile stress axis. As increasing fluence to 30 dpa, larger dislocation loops were clearly observed. In addition, the applied stress during irradiation effectively increased the number density of the loops on stressed planes comparing to less stressed planes. The average loop diameter was 7–9 nm independent on the relationship between stress axis and loop formed plane. Summary of microstructural evaluation is that 1) applied stress increased number density of loop on stressed planes and 2) the loops grow with increasing fluence.

### 5.3 Possible creep mechanism

Mechanism of radiation creep is discussed based on anisotropic microstructural evaluation during irradiation. Anisotropy was found in dislocation loops formation on  $\{111\}$  planes in this study. Those relatively large loops formed in irradiated SiC are likely Frank faulted loops [51]. Larger number of Frank loops on the stressed planes comparing to less stressed planes were clearly observed at  $\sim 500$  °C. Since forming Frank loop (additional planes) accounts for strain, observed anisotropy phenomenologically explains larger strain to stress direction, i.e. creep strain. However, it is difficult to quantitatively explain irradiation creep strain of SiC at this moment. This is because observed dislocation loops account for only small fraction of dimensional stability, i.e. swelling of CVD SiC. Assuming stoichiometric Frank loop formed in SiC, observed loops account for less than 10 % of macroscopic swelling of CVD SiC in this work.

Previous studies on irradiation creep of SiC at lower neutron fluences indicate that anisotropic formation of TEM-invisible (conventionally) defect clusters due to stress and they significantly contribute to the creep strain [51, 54]. That is also the case for this study. Since recent ion irradiation study indicates that the orientation of SIA loops and clusters is determined very early stage of irradiation [54], the observed anisotropic loop formation with relatively large size show possible anisotropic formation of small defect clusters. In conclusion, this study indirectly shows that anisotropic formation of small defect clusters due to applied stress and the significant contribution of that anisotropy to irradiation creep strain of SiC.

### 5.4 Summary of results

Neutron irradiation creep behavior of CVD SiC at 380 to 540 °C up to 30 dpa is reasonably explained with simultaneous swelling-creep coupling based on anisotropic SIA defect formation and secondary creep with constant creep rate. Applied stress effectively increases number density of loops on stressed  $\{111\}$  planes in the creep specimen. Analysis on creep behavior and microstructural observation indirectly show that anisotropic formation of small defect clusters due to applied stress and significant contribution of that anisotropy to irradiation creep strain of SiC.

## 6 Publications resulting from this work

[1] *High-resolution scanning transmission electron microscopy study of black spot defects in ion irradiated silicon carbide*, L. He, Y. Zhai, C. Liu, C. Jiang, I. Szlufarska, B. Tyburska-Puschel, K. Sridharan, P. Voyles, **Microscopy and Microanalysis**, 20, 1824-1825 (2014)

[2] *Atomic resolution imaging of black spot defects in ion irradiated silicon carbide*, L. He, H. Jiang, Y. Zhai, C. Liu, I. Szlufarska, B. Tyburska-Puschel, K. Sridharan, P. Voyles, **Microscopy and Microanalysis**, 21, 1337-1338 (2015)

[3] *Size distribution of black spot defects and their contribution to swelling in irradiated SiC*, B. Tyburska-Puschel, Y. Zhai, L. He, C. Liu, A. Boule, P. Voyles, I. Szlufarska, K. Sridharan, (2015) Submitted

[4] *Evolution of small clusters in Kr irradiated 3C-SiC: a combined cluster dynamics modeling and experimental study*, C. Liu, H. Li, Y. Zhai, B. Tyburska-Puschel, P. Voyles, K. Sridharan, D. Morgan, I. Szlufarska, To be submitted

[5] *Radiation-induced mobility of small defect clusters in covalent materials*, H. Jiang, L. He, P. Voyles, D. Morgan, I. Szlufarska, To be submitted (partial support from this grant).

## 7 References

1. Snead, L.L., et al., *Handbook of SiC properties for fuel performance modeling*. J. Nucl. Mater., 2007. **371**: p. 329.
2. Katoh, Y., et al., *Radiation effects in SiC for nuclear structural applications*. Submitted, 2011.
3. Snead, L.L., et al., *Handbook of SiC properties for fuel performance modeling*. Journal of Nuclear Materials, 2007. **371**(1–3): p. 329–377.
4. Devanathan, R. and W.J. Weber, *Displacement energy surface in 3C and 6H SiC*. Journal of Nuclear Materials, 2000. **278**(2–3): p. 258–265.
5. Stoller, R.E., et al., *On the use of SRIM for computing radiation damage exposure*. Nuclear Instruments and Methods in Physics Research Section B: Beam Interactions with Materials and Atoms, 2013. **310**: p. 75–80.
6. Ziegler, J.F., M.D. Ziegler, and J.P. Biersack, *SRIM - The stopping and range of ions in matter (2010)*. Nuclear Instruments & Methods in Physics Research Section B-Beam Interactions with Materials and Atoms, 2010. **268**(11–12): p. 1818–1823.
7. Y. Waseda, E.M., and K. Shinoda, *X-ray diffraction crystallography* Introduction, Examples and Solved Problems. Vol. 1. 2011, London New York: Springer Heidelberg Dordrecht
8. Leclerc, S., et al., *Strain-induced drift of interstitial atoms in SiC implanted with helium ions at elevated temperature*. Journal of Nuclear Materials, 2010. **397**(1–3): p. 132–134.
9. Barbot, J.F., A. Declémy, and M.-F. Beaufort, *Damage accumulation in He implanted SiC at different temperatures*. physica status solidi (a), 2013. **210**(1): p. 218–221.
10. Zang, H., et al., *Investigation of swelling induced by heavy ion and neutron irradiation in SiC*. Journal of Nuclear Materials, 2013. **433**(1–3): p. 378–381.
11. Barbot, J.F., M.F. Beaufort, and A. Declémy, *Strain build-up in SiC implanted at different temperatures*. Nuclear Instruments and Methods in Physics Research Section B: Beam Interactions with Materials and Atoms, 2014. **327**: p. 59–62.
12. Debelle, A. and A. Declémy, *XRD investigation of the strain/stress state of ion-irradiated crystals*. Nuclear Instruments and Methods in Physics Research Section B: Beam Interactions with Materials and Atoms, 2010. **268**(9): p. 1460–1465.
13. Kamitani, K., et al., *The elastic constants of silicon carbide: A Brillouin-scattering study of 4H and 6H SiC single crystals*. Journal of Applied Physics, 1997. **82**(6): p. 3152–3154.
14. Boule, A. and A. Debelle, *Strain-profile determination in ion-implanted single crystals using generalized simulated annealing*. Journal of Applied Crystallography, 2010. **43**(5 Part 1): p. 1046–1052.

15. Lin, Y.-R., et al., *Irradiation-induced microstructural evolution and swelling of 3C-SiC*. Journal of Nuclear Materials, 2015. **459**: p. 276-283.
16. Senor, D.J., et al., *Defect structure and evolution in silicon carbide irradiated to 1 dpa-SiC at 1100 °C*. Journal of Nuclear Materials, 2003. **317**(2-3): p. 145-159.
17. Price, R.J., *Neutron irradiation-induced voids in  $\beta$ -silicon carbide*. Journal of Nuclear Materials, 1973. **48**(1): p. 47-57.
18. Sawabe, T., et al., *Microstructure of heavily neutron-irradiated SiC after annealing up to 1500 °C*. Journal of Nuclear Materials, 2009. **386-388**: p. 333-337.
19. Newsome, G., et al., *Evaluation of neutron irradiated silicon carbide and silicon carbide composites*. Journal of Nuclear Materials, 2007. **371**(1-3): p. 76-89.
20. Katoh, Y., et al., *Microstructural development in cubic silicon carbide during irradiation at elevated temperatures*. Journal of Nuclear Materials, 2006. **351**(1-3): p. 228-240.
21. Jourdan, T., et al., *Influence of cluster mobility on Cu precipitation in  $\alpha$ -Fe: A cluster dynamics modeling*. Acta Materialia, 2010. **58**(9): p. 3400-3405.
22. Clouet, E., et al., *Precipitation kinetics of Al<sub>3</sub>Zr and Al<sub>3</sub>Sc in aluminum alloys modeled with cluster dynamics*. Acta Materialia, 2005. **53**(8): p. 2313-2325.
23. Swaminathan, N., et al., *Effects of grain size and grain boundaries on defect production in nanocrystalline 3C-SiC*. Acta Materialia, 2010. **58**(8): p. 2843-2853.
24. Bockstedte, M., A. Mattausch, and O. Pankratov, *Ab initio study of the migration of intrinsic defects in 3C-SiC*. Physical Review B, 2003. **68**(20): p. 205201-205201.
25. Slezov, V.V., *Basic Equations: Determination of the Coefficients of Emission in Nucleation Theory*, in *Kinetics of First-Order Phase Transitions*. 2009, Wiley-VCH Verlag GmbH & Co. KGaA. p. 7-38.
26. Jiang, C., D. Morgan, and I. Szlufarska, *Carbon tri-interstitial defect: A model for the D<sub>II</sub> center*. Physical Review B, 2012. **86**(14): p. 144118-144118.
27. Watanabe, Y., K. Morishita, and A. Kohyama, *Composition dependence of formation energy of self-interstitial atom clusters in  $\beta$ -SiC: Molecular dynamics and molecular statics calculations*. Journal of Nuclear Materials, 2011. **417**(1-3): p. 1119-1122.
28. Was, G.S., *The Damage Cascade*, in *Fundamentals of radiation materials science*. 2007, Springer Berlin Heidelberg. p. 125-154.
29. Rehn, L.E., P.R. Okamoto, and R.S. Averback, *Relative efficiencies of different ions for producing freely migrating defects*. Physical Review B, 1984. **30**(6): p. 3073-3080.
30. Naundorf, V., M.P. Macht, and H. Wollenberger, *Production-Rate of Freely Migrating Defects for Ion Irradiation*. Journal of Nuclear Materials, 1992. **186**(3): p. 227-236.
31. Kimoto, T., C.W. Allen, and L.E. Rehn, *Growth rate of dislocation loop in Fe-Ni-Cr alloy under Kr<sup>+</sup> ion and electron irradiation*. Journal of Nuclear Materials, 1992. **191-194**: p. 1194-1197.
32. Muroga, T., et al., *Free Defect Production Efficiency for Heavy-Ion Irradiation Estimated by Loop Growth Measurements*. Journal of Nuclear Materials, 1994. **212**: p. 203-206.



33. Gao, F. and W. Weber, *Atomic-scale simulation of 50 keV Si displacement cascades in  $\beta$ -SiC*. Physical Review B, 2000. **63**(5): p. 054101-054101.
34. Devanathan, R., W.J. Weber, and F. Gao, *Atomic scale simulation of defect production in irradiated 3C-SiC*. Journal of Applied Physics, 2001. **90**(5): p. 2303-2303.
35. Weber, W.J., et al., *The efficiency of damage production in silicon carbide*. Nuclear Instruments and Methods in Physics Research Section B: Beam Interactions with Materials and Atoms, 2004. **218**: p. 68-73.
36. Broeders, C.H.M. and a.Y. Konobeyev, *Defect production efficiency in metals under neutron irradiation*. Journal of Nuclear Materials, 2004. **328**: p. 197-214.
37. Malerba, L., *Molecular dynamics simulation of displacement cascades in  $\alpha$ -Fe: A critical review*. Journal of Nuclear Materials, 2006. **351**(1-3): p. 28-38.
38. Iwai, T., et al., *A positron beam study on vacancy formation in iron by ion beam irradiation at low temperature*. Journal of Physics: Conference Series, 2010. **225**: p. 012023.
39. Iwai, T., et al., *Defect formation in iron by MeV ion beam investigated with a positron beam and electrical resistivity measurement*. Nuclear Instruments and Methods in Physics Research Section B: Beam Interactions with Materials and Atoms, 2013. **315**: p. 153-156.
40. Iwai, T. and H. Tsuchida, *In situ positron beam Doppler broadening measurement of ion-irradiated metals - Current status and potential*. Nuclear Instruments and Methods in Physics Research, Section B: Beam Interactions with Materials and Atoms, 2012. **285**: p. 18-23.
41. Golubov, S.I., *1.13 - Radiation Damage Theory.pdf*. 2012. p. 357-391.
42. Stoller, R.E., et al., *Mean field rate theory and object kinetic Monte Carlo: A comparison of kinetic models*. Journal of Nuclear Materials, 2008. **382**(2-3): p. 77-90.
43. Xu, D., et al., *Combining in situ transmission electron microscopy irradiation experiments with cluster dynamics modeling to study nanoscale defect agglomeration in structural metals*. Acta Materialia, 2012. **60**(10): p. 4286-4302.
44. Xu, D. and B.D. Wirth, *Modeling spatially dependent kinetics of helium desorption in BCC iron following He ion implantation*. Journal of Nuclear Materials, 2010. **403**(1-3): p. 184-190.
45. Meslin, E., B. Radiguet, and M. Loyer-Prost, *Radiation-induced precipitation in a ferritic model alloy: An experimental and theoretical study*. Acta Materialia, 2013. **61**(16): p. 6246-6254.
46. Meslin, E., et al., *Cluster-dynamics modelling of defects in  $\alpha$ -iron under cascade damage conditions*. Journal of Nuclear Materials, 2008. **382**(2-3): p. 190-196.
47. Swaminathan, N., et al., *Radiation interaction with tilt grain boundaries in  $\beta$ -SiC*. Journal of Applied Physics, 2012. **111**(5): p. 054918-054918.
48. Yano, T., et al., *X-ray diffractometry and high-resolution electron microscopy of neutron-irradiated SiC to a fluence of  $1.9 \times 10^{27}$  n/m<sup>2</sup>*. Journal of Nuclear Materials, 1998. **253**: p. 78-86.

49. Weber, W.J., et al., *Ion-beam induced defects and nanoscale amorphous clusters in silicon carbide*. Nuclear Instruments and Methods in Physics Research Section B: Beam Interactions with Materials and Atoms, 2004. **216**: p. 25-35.
50. Jiang, H., et al., *Accelerated atomistic simulation study on the stability and mobility of carbon tri-interstitial cluster in cubic SiC*. Computational Materials Science, 2014. **89**: p. 182-188.
51. Katoh, Y., et al., *Observation and possible mechanism of irradiation induced creep in ceramics*. Journal of Nuclear Materials, 2013. **434**(1-3): p. 141-151.
52. Morscher, G.N. and J.A. Dicarlo, *A Simple Test for Thermomechanical Evaluation of Ceramic Fibers*. Journal of the American Ceramic Society, 1992. **75**(1): p. 136-140.
53. Katoh, Y., S. Kondo, and L.L. Snead, *Microstructures of beta-silicon carbide after irradiation creep deformation at elevated temperatures*. Journal of Nuclear Materials, 2008. **382**(2-3): p. 170-175.
54. Katoh, Y., et al., *High-dose neutron irradiation of Hi-Nicalon Type S silicon carbide composites. Part 2: Mechanical and physical properties*. Journal of Nuclear Materials, 2015. **462**: p. 450-457.

# Role of Defects in Swelling and Creep of Irradiated SiC

## OVERVIEW

### Purpose:

Perform an integrated experimental and modeling research to discover the previously invisible defects in irradiated SiC and to determine the contributions of these defects to radiation swelling and radiation creep.

### Objectives:

- Analyze neutron, self-ion and possibly inert gas irradiated single crystal and polycrystalline SiC samples to identify defect structures
- Apply STEM imaging simulation technique to characterize clusters point defects that comprise the clusters visible in conventional TEM in 3C SiC.
- Assess concentration of detectable point defects in ion irradiated 3C-SiC as a function of dose, temperature, and ion species on selected samples.
- Develop a model for evolution of defect clusters in irradiated SiC and determine the contribution from these clusters to radiation-induced swelling under conditions relevant to Light Water Reactors(LWR)

## DETAILS

**Principal Investigator:** Izabela Szlufarska

**Institution:** University of Wisconsin - Madison

**Collaborators:** Prof. James Blanchard (UW), Prof. Paul Voyles (UW), Prof. Kumar Sridharan (UW), Dr. Yutai Katoh (ORNL)

**Duration:** September 2012-September 2015

**Total Funding Level:** \$875,350

**TPOC:** Dr. Yutai Katoh (ORNL)

**Federal Manager:** Dr. Rich Reister

**Workscope:** LWRS-4

**PICSNE Workpackage #:**

Project number 12-3357

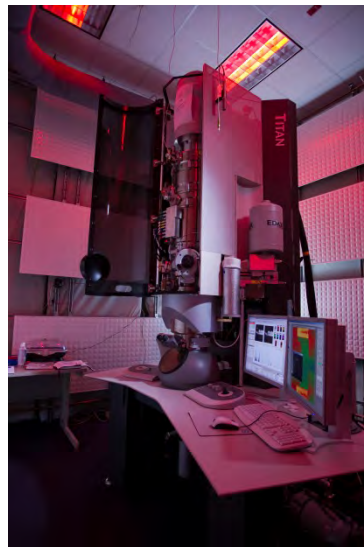
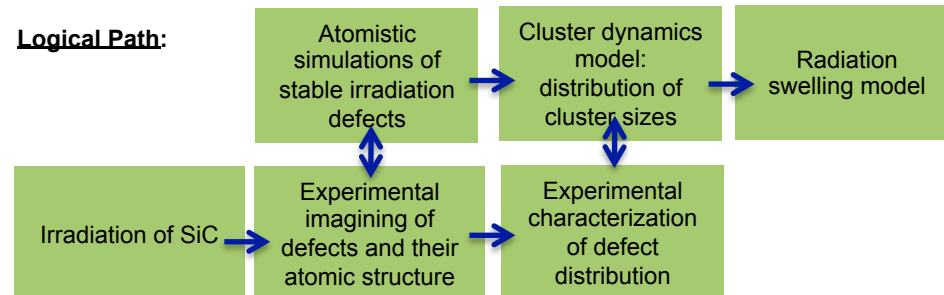


Figure 1 Aberration corrected STEM (FEI TITAN)

## IMPACT

### Logical Path:



### Outcomes:

- Knowledge of the most stable defect structures and the rate controlling processes during defect evolution is essential for development of predictive models for swelling and creep as a function of temperature and radiation dose.
- The proposed research will lay the essential groundwork for adoption of SiC in light-water reactors, including rigorous design of SiC-based composites for fuel cladding.

